Journal of Materials Science & Technology 97 (2022) 176–181

Contents lists available at ScienceDirect

Journal of Materials Science & Technology

journal homepage: www.elsevier.com/locate/jmst

Letter

Extraordinary toughening enhancement in nonstoichiometric vanadium carbide

1. Introduction

Fracture toughness is the ability of materials against both the initiation and propagation of cracks [1], which is a crucial mechanical property for safety-critical applications of structural materials. Although the yield strength of ceramics is significantly higher than that of metallic materials, the fracture toughness is severely lower than that of metallic materials due to the strongly directional covalent bonding [1–3]. For a long time, how to improve the fracture toughness of ceramics without the deterioration of strength (or hardness) has been one of the most challenging problems in materials science. It has been known for decades that some mechanisms (strain-induced phase transformation, bridging and crack deflection or meandering) of extrinsic toughening in ceramics have been established [4,5]. These toughening mechanisms are essentially based on increasing the energy dissipation during crack propagation. Since the 1980s, extensive experimental research demonstrates that fracture toughness can multiply by stress-induced phase transformation (such as the tetragonal-to-monoclinic transformation of ZrO_2 [6,7] and bridging of in-situ generated whiskers (β-Si_3N_4 or SiC) [8,9] or by adding flexible carbons (carbon nanotubes or graphene) [10,11] during crack propagation. With the high-fraction second phase of β-Si_3N_4 or SiC whiskers or tetragonal ZrO_2, the fracture toughness of Al_2O_3-based composites are remarkably increased to 8-13 MPa $m^{1/2}$ [12–14], even close to that of the intermetallic Ti_3Al [15]. However, for refractory transition metal carbides (RTMCs), compounding with ZrO_2, β-Si_3N_4 or SiC whiskers does not realize dramatic enhancement in toughness, but resulting in a serious deterioration in hardness [16–18].

RTMCs have been widely used as structural materials, cutting tools, catalysts, etc., because of the attractive chemical and physical properties, such as high thermal and electric conductivity, excellent chemical and thermal stability, and outstanding hardness [2,3]. However, RTMCs are notoriously brittle and can be subject to catastrophic failure from the growth of a single dominant crack, which has greatly limited their applications and development [3]. To improve the fracture toughness and facilitate densification, metals (Co, Ni, or Fe) are generally used as binders for manufacturing high-toughness RTMCs, referred to as cermets [19]. Although cermets have a high fracture toughness of more than 10 MPa $m^{1/2}$ and have been widely used commercially, especially WC-Co cermets, the incorporation of high-concentration metallic binders inevitably leads to a serious deterioration of hardness and thermal stability [20,21]. To achieve a combination of high fracture toughness and hardness in RTMCs, the current strategies are nanonization and dispersion toughening by compounding with other high-hardness covalent compounds, based on deflection and meandering of cracks [22–24]. However, the presented results show that the dispersion toughening is not optimal in RTMC-based composites, and even the fracture toughness of some WC-based carbides with VC, ZrC, or TiC is lower than that of pure WC [25–27].

Hence, exploring effectual toughening approaches is urgent to design RTMCs with combinations of high hardness and toughness. Here we first report a doubling of fracture toughness in RTMCs without any toughened second phase. We synthesized nonstoichiometric VC_{1-x} ($0.4 \leq 1-x \leq 0.6$) by mechanical alloying (MA) followed by densification via spark plasma sintering (SPS). Compared with stoichiometric VC, the fracture toughness of VC_{1-x} increases from 3.4 to 6.3-7.3 MPa $m^{1/2}$, close to that of the binderless ultrafine WC (the toughest binary carbide) [28–30]. The microstructure characterization and crack propagation behavior analysis indicates that the extraordinary toughening enhancement is attributed to a novel strategy combined with coherency toughening and amorphous bridging toughening. The synthesized VC_{1-x} ($0.5 \leq 1-x \leq 0.6$) have a quasi-monophasic microstructure with the carbon-rich matrix and carbon-poor precipitates. The matrix and precipitates have the same rock-salt structure with stoichiometric VC and have completely coherent interfaces. The strong coherent interfaces make a transgranular fracture feature and crack deflection near coherent nanoprecipitates, leading to toughening through increasing fracture energy and lengthening the path of crack propagation. Moreover, the amorphous bridging caused by high-concentration carbon vacancies in VC_{1-x} shows a great resistance to crack propagation, contributing to further toughening. Our discovery of the coherency toughening and amorphous bridging toughening provides a new strategy for breaking through the strength (hardness)-toughness limit of strong covalent compounds (carbides, borides, nitrides, and oxides).

2. Experimental

2.1. Materials and preparation

Nonstoichiometric VC_{1-x} ($0.4 \leq 1-x \leq 0.6$) powders were synthesized through mechanical alloying (MA). Commercially available V and VC powers (purity: 99.5%, Qinhuangdao ENO High-tech Material Development CO. Ltd., China) with a particle size between 1-3 μm were utilized as the raw materials. The compositions of raw materials listed in Table S1 were weighed and sealed in WC vessel in an argon atmosphere with WC balls and then ball-milled in a planetary milling system (Pulverisette4, FRITSCH, Germany) at 600 r/min. The ball to powder weight ratio was selected as 10:1. The milling VC_{1-x} were performed at room temperature for 30 h with 0.5 h cool-off periods after 2 h segments to avoid overheating. Afterwards, the milled powders were annealed in a vacuum carbon tube furnace (VVSgr-40-2000, Shanghai, China) at 600 °C for 1 h. Sample bulks were synthesized via spark plasma sintering

https://doi.org/10.1016/j.jmst.2021.04.057

(SPS, LABOX^{TM}-110, Sinter Land Inc., Japan) technique. The powder mixtures were loaded into a graphite die and sintered under an argon atmosphere at 1200-1500°C for 10 min. A heating rate of 50°C min^{-1} was selected, and a pressure of 40 MPa was applied on the compact throughout the sintering process.

2.2. Microstructural characterization

Phase identification was carried out by an X-ray diffractometer (XRD, D/max-2500PC, Rigaku, Japan) with CuK_α radiation (λ=0.15406 nm) at 40 kV and 200 mA. The XRD curves of the specimens were recorded from 30° to 80° with a step size of 0.02° (2θ) and a counting time of 1 s. Microstructural characterization was analyzed with a scanning electron microscopy (SEM, FEI Scios, America) in backscattered electron (BSE) mode. The SEM was fitted with energy-dispersive X-ray spectroscopy (EDS), and commercially available VC was used to calibrate it. The grain size and phase volume fraction of intergranular/intragranular precipitates were analyzed using the ImageJ program [31]. For SEM observation, the samples were polished through mechanical polishing followed by Ar-ion milling. The scanning transmission electron microscope (STEM, Talos F200X, America) was performed operating at 200 kV. Cross-sectional specimen for STEM observations was prepared by dual-beam focused ion beam (FIB) scanning microscopy (Versa 3D, FEI, America) using Ga-ion beam and accelerating voltage ranging from 2 to 40 kV, followed by ion-milling (Gatan 691, Gatan, America) operated from 1.5 to 0.5 kV. And then argon plasma cleaning (Solarus 950, Gatan, America) was used to remove completely any residual amorphous film. To observe the fracture behavior of the specimen, the STEM foil of $VC_{0.5}$ was prepared at the crack tip, as shown in Fig. S1 in Supporting Information. For comparison, the stoichiometric VC foil was also prepared in the same manner. The lattice mismatch value was calculated by the STEM analysis form the interplanar spacing. The equation can be described as: $\delta = 2(a_{precipitate}-a_{matrix})/(a_{precipitate}+a_{matrix})$, where a refers to the lattice parameter of each phase [32].

2.3. Mechanical property measurements

Vickers hardness (H_V) testing was conducted on the polished surface using a Vickers diamond indenter (FM700, Future-Tech, Japan) with a load of 500 g and a holding time of 10 s. Hv was determined from the Eq. (1):

$$H_V = 1854.4F/L^2 \quad (1)$$

where F is the applied load and L is the arithmetic mean of the two diagonals of the Vickers indentation. The fracture toughness was determined by the Vickers indentation method and single-edge notched beam (SENB) tests. The indentation fracture toughness measurement was carried out with a load of 5000 g and a holding time of 10 s. The fracture toughness (K_{IC}) was calculated by using Shetty's equation [33]:

$$K_{IC} = 0.0889(H_V P/41)^{1/2} \quad (2)$$

where H_V is the Vickers hardness, P is the indentation load and l is the crack length. Each hardness and indentation toughness value represented an average of at least ten points. SENB tests were performed using a three-point bending tester (DZS-II, China Building Material Test & Certification Group Co., Ltd., China) with a loading velocity of 0.05 mm/min and a span of 16 mm. Fracture toughness can be determined using Eq. (3) [34]:

$$K_{IC} = Y\frac{3PL}{2BW^2}c^{1/2} \quad (3)$$

where P is the bending load, c is the length of the notch, B and W are the width and height of the sample, respectively. L is the span between two lower supporting points and Y is usually defined as c/W. In the case of L/W =4, Y can be represented as Eq. (4) [34]:

$$Y = 1.93 - 3.07\frac{c}{W} + 14.53\left(\frac{c}{W}\right)^2 - 25.07\left(\frac{c}{W}\right)^3 + 25.8\left(\frac{c}{W}\right)^4 \quad (4)$$

The SENB specimens were first cut using Wire Cut Electrical Discharge Machining (WEDM, DK7720, Fangzheng CNC Machine Tool Co., LTD, China) and then polished with 2.5 μm diamond paste before bending tests. The dimensions of the specimens were 18 mm × 4 mm × 2 mm specified in ASTM Standard E1820-05a [34]. The pre-notch with length of 2 mm was made by a 0.2 mm thick diamond wafer, whose direction was perpendicular to the length direction of the specimen. The schematic of the SENB specimen is shown in Fig. S2. Three bar samples were tested for each material.

3. Results and discussion

3.1. Phase detection and microstructural characterizations

In high-hardness RTMCs, anion vacancies are ubiquitous in transition metal carbides and nitrides and previous studies have confirmed that high-dose vacancies (over 70%) still do not cause structural instability [35–37]. In this study, we also synthesized VC_{1-x} ($0.4 \le 1-x \le 0.6$) with high-concentration carbon vacancies through MA and subsequent SPS. After milling of V and VC powders with the specified ratio (Table S1), single-phase nonstoichiometric VC_{1-x} ($0.4 \le 1-x \le 0.6$) powders were obtained, which is determined by XRD analysis (as shown in Fig. S3 and see more details in supplementary materials). Using 30 h-milled VC_{1-x} powders as starting materials, dense nonstoichiometric VC_{1-x} bulks were synthesized by SPS at temperatures of 1200-1500 °C. Fig. 1(a) shows the XRD pattern of the nonstoichiometric $VC_{0.5}$ bulk after sintering at 1400°C, indicating a single-phase rock-salt structure ($Fm\bar{3}m$). By Rietveld refinement with the FullProf program [38], the lattice parameter of $VC_{0.5}$ is 4.145 Å, slightly smaller than that of stoichiometric VC (4.175 Å) [39]. The obtained $VC_{0.6}$ bulks also show a single-phase rock-salt structure, however, a second phase of hexagonal V_2C (h-V_2C) is observed in $VC_{0.4}$ with higher-density carbon vacancies (Fig. S4). Although the XRD results clearly indicate that the synthesized VC_{1-x} ($0.5 \le 1-x \le 0.6$) bulks are single-phase, the back-scattered electron (BSE) images (Figs. 1(b) and S5) exhibit a typical biphasic feature. Numerous intergranular/intragranular precipitates (dark region) are found, referring to a second phase with low density. Moreover, quantification (see inset of Fig. 1(b)) and distribution analyses of V and C atoms (Fig. 1(c and d)) show that the biphasic structure is caused by the concentration fluctuation of C. In the synthesized $VC_{0.5}$ bulk, the matrix is micron-sized carbon-rich $VC_{0.60}$, and the precipitate phase is multi-scale carbon-poor $VC_{0.37}$ distinguished as intergranular submicron phase and intragranular nanoprecipitates (NPs). The energy-dispersive X-ray spectroscopy (EDS) results of nonstoichiometric VC_{1-x} seem to be contrary to the single-phase structure feature observed from XRD analysis (Figs. 1(a) and S4), which may be due to the overlap of diffraction peaks and thus means that the carbon-poor precipitates should have the same crystal structure as the carbon-rich matrix and similar lattice parameters.

3.2. TEM analysis

To further understand the microstructures of the synthesized $VC_{0.5}$ bulks, a detailed transmission electron microscopy (TEM) characterization was employed. Fig. 2(a–c) shows the high angle annular dark field (HADDF) scanning TEM (STEM) image and corresponding EDS mappings. In consistent with the SEM-EDS results, the carbon-poor $VC_{0.37}$ existing as isolated intragranular

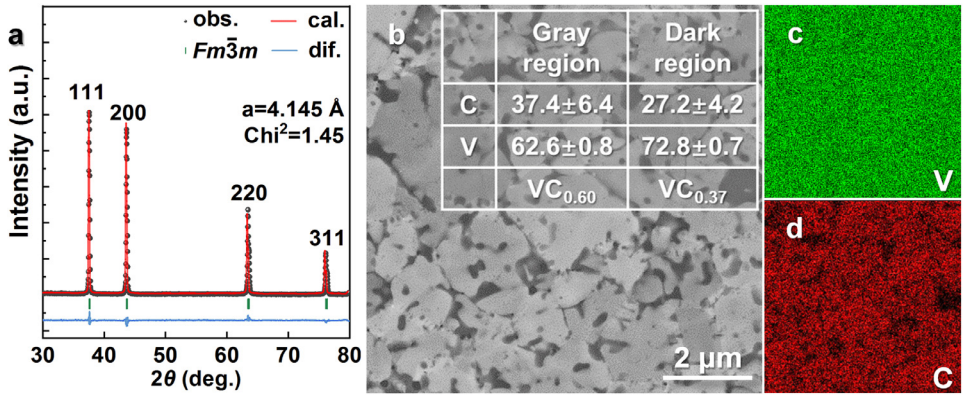

Fig. 1. Analyses of crystal structure, chemical composition, and microstructural characterizations. (a) Rietveld refinement for XRD pattern of nonstoichiometric $VC_{0.5}$ bulk after sintering at 1400 °C. (b) Typical BSE image and energy-dispersive x-ray spectroscopy (EDS) point-analyzed results in the inset. (c, d) The corresponding SEM-EDS mappings of (a).

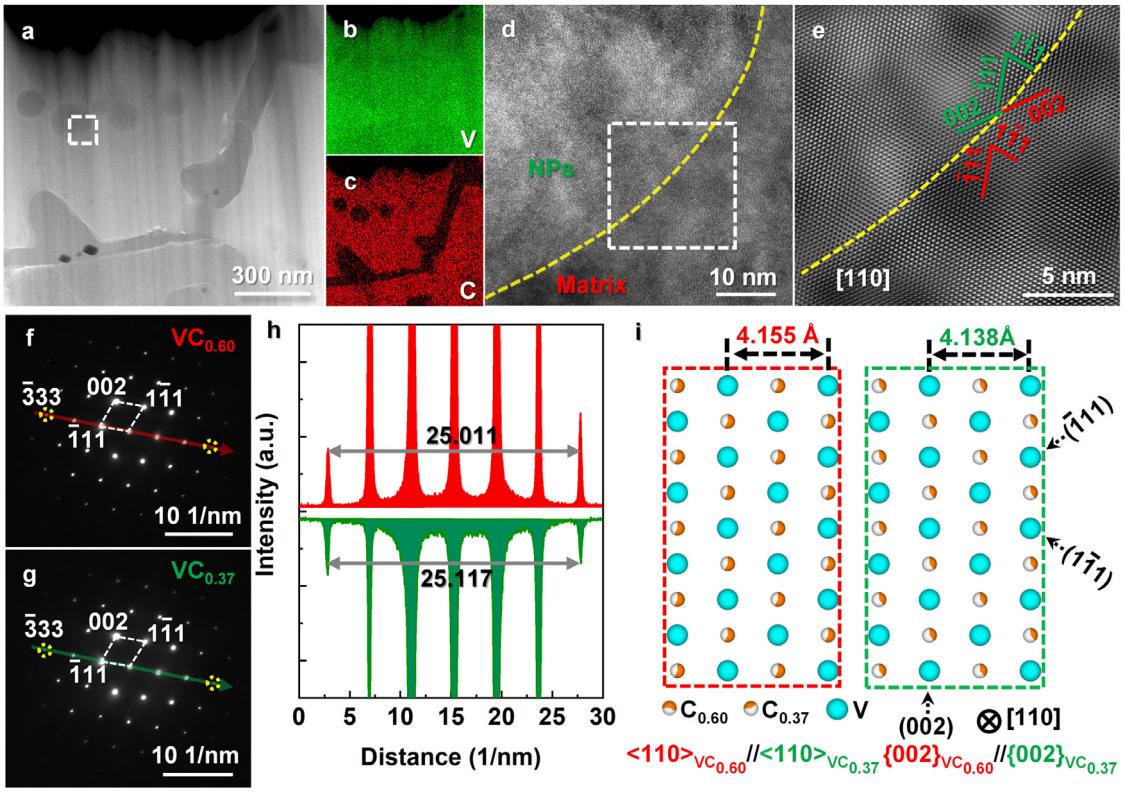

Fig. 2. TEM analysis and quasi-monophasic structure model of the synthesized $VC_{0.5}$. (a) HAADF-STEM image of the $VC_{0.5}$ bulk sintered at 1400 °C. (b, c) EDS mappings acquired from (a). (d) Typical HRTEM image acquired from the marked area of (a). (e) The IFFT image corresponding to the marked area of (d). (f, g) SAED patterns of (f) $VC_{0.60}$ matrix and (g) $VC_{0.37}$ precipitates. (h) Intensity-distance profiles are taken from the SAED patterns of the matrix and precipitates, as indicated by the red and green arrows in (f) and (g), respectively. (i) Atomic structure projection of synthesized $VC_{0.5}$ along the [110] zone axis.

NPs and shell-like intergranular precipitates are scattered in the carbon-rich $VC_{0.60}$ matrix. Figs. 2(d, e) and S6 show high-resolution transmission electron microscopy (HRTEM) images of the matrix and intergranular/intragranular precipitates and the corresponding inverse Fast Fourier transformation (IFFT) images. Interestingly, we found that the carbon-poor $VC_{0.37}$ precipitates are precisely coherent with the adjacent carbon-rich $VC_{0.60}$ matrix. As shown in Figs. 2(e) and S6, both the matrix and the precipitates have same the rock-salt structure and orientation relationships of $<110>_{VC_{0.60}}//<110>_{VC_{0.37}}$ and $\{002\}_{VC_{0.60}}//\{002\}_{VC_{0.37}}$. The selected area electron diffraction (SAED) patterns (Fig. 2(f and g)) of the $VC_{0.60}$ matrix and $VC_{0.37}$ precipitates seem to be the same. However, some concomitant diffraction spots are observed in the SAED pattern collected near the coherent interfaces (Fig. S7), suggesting a small difference in the lattice parameters of the matrix and precipitates. The lattice parameters of the $VC_{0.6}$ matrix and $VC_{0.37}$ precipitates are 4.155 Å and 4.138 Å, respectively, calculated from the interplanar spacing of $(\bar{3}33)$ (Fig. 2(h)). Herein, it is verified that the undetected diffraction peaks of the carbon-poor $VC_{0.37}$ precipitates in XRD profile (Fig. 1(a)) are due to the same crystal structure and almost identical lattice parameters with the carbon-rich $VC_{0.60}$ matrix. From the above, we undoubtedly confirm that the synthesized VC_{1-x} ($0.5 \leq 1\text{-}x \leq 0.6$) bulks are formed from the carbon-rich matrix and coherent carbon-poor precipitates with the

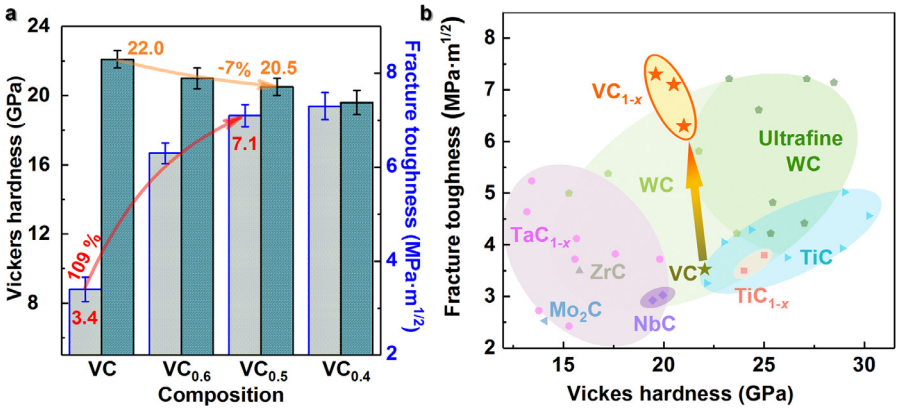

Fig. 3. Comparison of mechanical properties. (a) Vickers hardness and fracture toughness of VC_{1-x} at 1400 °C. (b) Ashby plot of hardness against fracture toughness for VC_{1-x} compared with the previously reported binary RTMCs. Error bars shown in the plot represent the standard deviation of the data.

same crystal structure and similar lattice parameters. Since there is no essential change in the crystal structure and chemical composition between the presented two phases, we named the synthesized VC_{1-x} ($0.5 \leq 1\text{-}x \leq 0.6$) as quasi-monophasic ceramic to distinguish it from the traditional dual-phase ceramics. Fig. 2(i) presents the quasi-monophasic structure model of the synthesized $VC_{0.5}$. The carbon-rich $VC_{0.60}$ matrix and carbon-poor $VC_{0.37}$ precipitates have the same rock-salt structure and have completely coherent interfaces with a small lattice mismatch of 0.4%.

3.3. Mechanical properties

Fig. 3 displays the mechanical properties of nonstoichiometric VC_{1-x} ($0.4 \leq 1\text{-}x \leq 0.6$) and stoichiometric VC. Like conventional covalent RTMCs [2,3], stoichiometric VC has high hardness of 22.1±0.5 GPa but low fracture toughness of 3.4±0.3 MPa $m^{1/2}$ (Fig. 3(a)). Compared with the stoichiometric VC, VC_{1-x} show a slight decrease in hardness, accompanied by a huge increase in fracture toughness. Significantly, the $VC_{0.5}$ shows a good trade-off of the microhardness (20.5±0.5 GPa) and fracture toughness (7.1±0.2 MPa $m^{1/2}$). The fracture toughness of $VC_{0.5}$ increases by more than 100% with only 7% hardness loss, compared with that of the VC. It is well known that nearly 100% toughening in the commercial WC-Co cermet is often achieved by sacrificing more than 30% hardness [20]. Higher-concentration carbon vacancies result in a continuous toughening. In $VC_{0.4}$, the fracture toughness is increased up to 7.3±0.3 MPa $m^{1/2}$ (115% higher than that of the VC), however, the hardness is reduced to less than 20 GPa, which may be due to the presence of soft phase h-V_2C [40]. We also measured Vickers indentation fracture toughness, as shown in Fig. S8. Although the indentation toughness values are systemically lower than the SENB ones (by about 10%), the relative difference in toughness between VC and our nonstoichiometric VC_{1-x} ($0.4 \leq 1\text{-}x \leq 0.6$) is almost consistent in these two methods (Fig. S9). In Fig. 3(b), we summarize the microhardness and fracture toughness of VC_{1-x} and the typical binary monophasic RTMCs [28–30,36,41–51]. Among these binary RTMCs, the hexagonal WC has superior hardness and fracture toughness. The ultrafine WC is the hardest and toughest binary RTMCs currently reported [28–30]. In difference with WC, the fracture toughness of VC and other cubic binary RTMCs are less than 5 MPa $m^{1/2}$, even for the ultrafine TiC [51]. Surprisingly, without any addition of the toughening phase, the fracture toughness of our synthesized VC_{1-x} can be increased multiply. In particular, even if the grain size of the matrix is mainly micron-scaled (Fig. S5), the toughness of $VC_{0.5}$ is still close to that of the ultrafine WC.

3.4. Fracture behavior

To understand the extraordinary toughening enhancement in nonstoichiometric VC_{1-x}, we analyzed the fracture behaviors via SEM and TEM. Figs. 4(a, b) and S10(a, b) display the representative BSE images of a radial crack generated by Vickers indentation on the polished surface of $VC_{0.5}$. Notably, intergranular fracture feature is almost invisible in the sample of $VC_{0.5}$. The fracture surface also shows an unadulterated step-like transgranular fracture (STF) (Fig. S10(c)), while the transgranular fracture occurs locally in stoichiometric VC (Fig. S10(d)). Reasonably, the STF feature should be due to the strong coherent interfaces between the matrix and precipitates. For the metallic system, it has been widely demonstrated that the presence of coherent precipitates with small lattice misfit can effectively strengthen materials by the reinforced interfaces between matrix and precipitates [52–54]. Herein, the strong coherent interfaces in nonstoichiometric VC_{1-x} mainly contribute to the improvement of fracture toughness. In most of single-phase or composite ceramics, the conventional grain or phase boundaries have lower strength than that of grains, resulting in low fracture energy and the intergranular-dominated fracture [10,36,41]. In nonstoichiometric VC_{1-x}, the strong coherent interfaces compel the cracks to propagate through the grains, which leads to an increase in the fracture energy and thus enhancement of the fracture toughness. Meanwhile, grain bridging and crack deflection indicated by the red and yellow arrows in Fig. 4(b and c), respectively, are also usually recognized as signs of toughening [4,5]. A small amount of WC impurities introduced during MA are observed (Fig. 4(b)), and their contribution to mechanical properties of VC_{1-x} is minuscule due to the negligible contents. In composite ceramics, the crack deflection occurs in a way that the crack bypasses the second phase and propagates along the weak phase boundaries, resulting in the extension of the crack propagation path to increase the fracture toughness [10,43,55]. However, there is an unusual crack deflection when cracks propagate in the nonstoichiometric VC_{1-x}. The HADDF-STEM image shows a noticeable crack deflection near the coherent NPs (Fig. 4(c)). With difference from that in conventional composites, the crack bypasses the coherent NPs by propagating in the matrix ~20 nm away from the coherent interfaces, resulting in an additional toughening. This unique crack deflection may be attributed to the local stress zone nearby the coherent interfaces caused by the small lattice mismatch.

Because of the unadulterated STF and transgranular-propagation crack deflection caused by the strong coherent interfaces, the nonstoichiometric VC_{1-x} shows a remarkable increase in fracture toughness. Regardless of the external toughening caused by the microstructures, the fracture toughness of materials is intrinsically

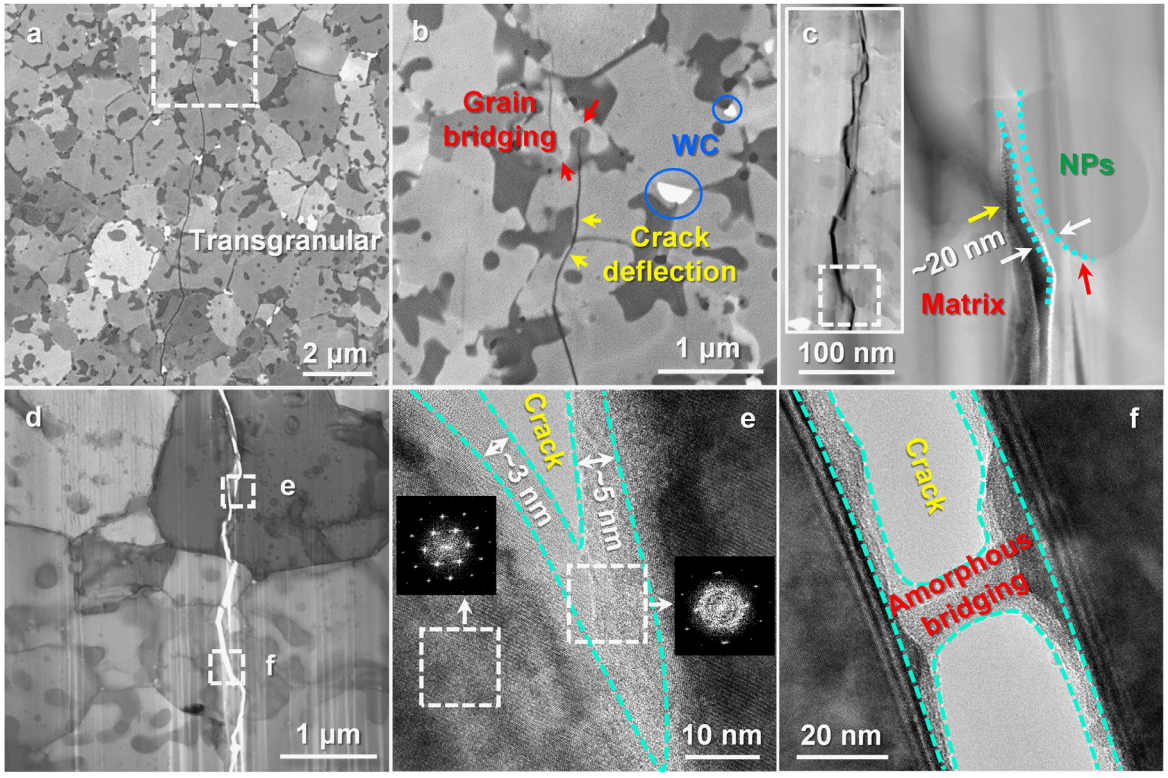

Fig. 4. Analysis of fracture behaviors. (a) The BSE image of the cracks initiated during indentation of $VC_{0.5}$. (b) Magnified BSE image from the marked region in (a). Minor WC impurity introduced during MA are observed. (c) HADDF-STEM image of the cracks. (d) BF-STEM image of the crack propagation path in $VC_{0.5}$. (e) Typical HRTEM image of the crack tip acquired from the marked of (d). Insets: the corresponding Fast Fourier transformation (FFT) images of the marked areas. (f) HRTEM image of the crack marked in (d).

determined by the chemical composition and crystal structure, related to the propagation behaviors of cracks in grains. Figs. 4(d, f) and S11-S12 show the typical BF-STEM and HRTEM images of cracks in grains of nonstoichiometric $VC_{0.5}$ and stoichiometric VC. Clearly, we can find amorphous layers with thicknesses of 3-5 nm on the crack surfaces of $VC_{0.5}$, attributed to stress-induced amorphization in covalent materials [56]. Unlike metals, because of the obvious orientation of covalent bonding, the plastic deformation of covalent materials is macroscopically imperceptible and is achieved by stress-induced amorphization or phase transformation instead of dislocation movement, unless stress is applied in a specific direction [56,57]. Similar amorphous layers are also observed on the fracture surfaces of the stoichiometric VC (Fig. S12(b)). However, it is surprising that numerous amorphous bridges between cracks of $VC_{0.5}$ are found, as shown in Figs. 4(f) and S11. As we know, the bridging formed with whiskers (β-Si_3N_4 or SiC) or flexible carbons (carbon nanotube or graphene) is one of the most effective toughening strategies in ceramics, which will impede crack extension and contribute to the fracture resistance [10,11,55]. Similarly, the amorphous bridging in $VC_{0.5}$ contributes to the toughening enhancement. In the stoichiometric VC, no amorphous bridging is observed (Fig. S12), suggesting that the formation of amorphous bridging in nonstoichiometric VC_{1-x} is related to the high-concentration carbon vacancies.

4. Conclusion

In summary, we realize superb toughening enhancement in nonstoichiometric VC_{1-x} ($0.4 \leq 1\text{-}x \leq 0.6$), significantly, the $VC_{0.5}$ sintered at 1400°C has a good balance of high fracture toughness of 7.1±0.2 MPa $m^{1/2}$ and hardness of 20.5±0.5 GPa. The fracture toughness of $VC_{0.5}$ increases by more than 100% with a hardness loss of 7%, compared with that of stoichiometric VC. Determined by the structural characters of high-concentration carbon vacancies and unique quasi-monophasic microstructure with low-lattice-misfit coherent precipitates, the toughness enhancement of VC_{1-x} involves an innovative self-toughening strategy combined with coherency toughening and amorphous bridging toughening. The unadulterated STF and crack deflection caused by the strong coherent interfaces and the amorphous bridging caused by the high-concentration carbon vacancies all increase the energy dissipation in the crack propagation, thus resulting in the extraordinary toughening enhancement. Even so, we believe that the fracture toughness and hardness can be further improved by controlling the grain sizes of matrix and precipitates. Additionally, although the lattice-misfit coherent structure design has been successfully developed in many alloy systems, such as nanostructured alloys, steels, and also HEAs, it has not been reported in binary RTMCs until now. Thereby, understanding the origin of the coherent structure and extending it to other strongly covalent ceramics will be the next frontier.

Declaration of Competing Interest

The authors declare that they have no known competing financial interests or personal relationships that could have appeared to influence the work reported in this paper.

Acknowledgement

This work was financially supported by the Natural Science Foundation of Hebei Province of China (Nos. E2016203425 and E2017203223), the Key Projects of Scientific and Technological Research in Hebei Province (No. ZD2017074), the National Nat-

ural Science Foundation of China (No. 12075215) and the Science and Technology Project of Hebei Education Department (No. QN2021136 and ZD2017026) .

Supplementary materials

Supplementary material associated with this article can be found, in the online version, at doi:10.1016/j.jmst.2021.04.057.

References

[1] M.E. Launey, R.O. Ritchie, Adv. Mater. 21 (2009) 2103–2110.
[2] L.E Toth, Transition Metal Carbides and nitrides, Academic Press, New York, 1971.
[3] H.O. Pierson, Handbook of Refractory Carbides and Nitrides: Properties, Characteristics, Processing and Applications, William Andrew, New Jersey, 1996.
[4] R.O. Ritchie, Int. J. Fracture 100 (1999) 55–83.
[5] R.W. Steinbrech, J. Eur. Ceram. Soc. 10 (1992) 131–142.
[6] G.A. Evans, M.R. Cannon, Acta Metall. 34 (1986) 761–800.
[7] R.H. Dauskardt, W. Yu, R.O. Ritchie, J. Am. Ceram. Soc. 70 (2010) 248–252.
[8] F.F. Lange, J. Am. Ceram. Soc. 62 (1979) 428–430.
[9] H.F. Wang, Y.B. Bi, N.S. Zhou, H.J. Zhang, Ceram. Int. 42 (2016) 727–733.
[10] Z. Xia, L. Riester, W.A. Curtin, H. Li, B.W. Sheldon, J. Liang, B. Chang, J.M. Xu, Acta Mater. 52 (2004) 931–944.
[11] J. Dusza, J. Morgiel, A. Duszová, L. Kvetková, M. Nosko, P. Kun, C. Balázsi, J. Eur. Ceram. Soc. 32 (2012) 3389–3397.
[12] N. Claussen, J. Am. Ceram. Soc. 59 (2010) 49–51.
[13] H.M. Jang, J.H. Moon, C.W. Jang, J. Am. Ceram. Soc. 75 (2010) 3369–3376.
[14] P.F. Becher, J. Am. Ceram. Soc. 74 (2010) 255–269.
[15] C. Leyens, M. Peters, Titanium and Titanium Alloys: Fundamentals and Applications, Wiley-VCH Verlag GmbH and Co. KGaA, Weinheim, 2003.
[16] B. Basu, J.H. Lee, D.Y. Kim, J. Am. Ceram. Soc. 87 (2004) 317–319.
[17] Z. Wang, J. Jia, L. Cao, N. Sun, Y. Wang, Materials 12 (2019) 1868.
[18] S. Sugiyama, D. Kudo, H. Taimatsu, Mater. Trans. 49 (2008) 1644–1649.
[19] E.H. Exner, Metall. Rev. 24 (1979) 149–173.
[20] K. Jia, T.E. Fischer, B. Gallois, Nanostruct. Mater. 10 (1998) 875–891.
[21] S. Lay, J. Vicens, F. Osterstock, J. Mater. Sci. 22 (1987) 1310–1322.
[22] Y. Yue, Y. Gao, W. Hu, B. Xu, J. Wang, X. Zhang, Q. Zhang, Y. Wang, B. Ge, Z. Yang, Z. Li, P. Ying, X. Liu, D. Yu, B. Wei, Z. Wang, X. Zhou, L. Guo, Y. Tian, Nature 582 (2020) 370–374.
[23] L. Cheng, Z. Xie, G. Liu, Ceram. Int. 39 (2013) 5077–5082.
[24] S.K. Sharma, B. Venkata Manoj Kumar, K. Lim, Y. Kim, S.K. Nath, Ceram. Int. 40 (2014) 6829–6839.
[25] S.G. Huang, K. Vanmeensel, O. Van der Biest, J. Vleugels, Int. J. Refract. Metals Hard Mater. 26 (2008) 41–47.
[26] A. Nino, Y. Izu, T. Sekine, S. Sugiyama, H. Taimatsu, Int. J. Refract. Metals Hard Mater. 69 (2017) 259–265.
[27] H.C. Kim, D.K. Kim, I.Y. Ko, I.J. Shon, J. Ceram. Process Res. 8 (2007) 91–97.
[28] S. Grasso, J. Poetschke, V. Richter, G. Maizza, Y. Sakka, M.J. Reece, J. Am. Ceram. Soc. 96 (2013) 1702–1705.
[29] H. Kim, I. Shon, J.E. Garay, Z.A. Munir, Int. J. Refract. Metals Hard Mater. 22 (2004) 257–264.
[30] H. Kim, D. Kim, K. Woo, I. Ko, I. Shon, Int. J. Refract. Metals Hard Mater. 26 (2008) 48–54.
[31] A. Ullah, G.Q. Liu, H. Wang, D.F. Khan, M. Khan, Chin. J. Stereol. Image Anal. 17 (2012) 301–312.
[32] B. Geddes, H. Leon, X. Huang, Superalloys: Alloying and Performance, ASM International, Flevoland, 2010.
[33] D.K. Shetty, I.G. Wright, P.N. Mincer, A.H. Clauer, J. Mater. Sci. 20 (1985) 1873–1882.
[34] Standard Test Method for Measurement of Fracture Toughness, ASTM International, West Conshohocken, PA, 2005.
[35] H.W. Hugosson, P.A. Korzhavyi, U. Jansson, B.S. Johansson, O. Eriksson, Phys. Rev. B 63 (2001) 165116.
[36] Z. Zhang, C. Geng, Y. Ke, C. Li, X. Jiao, Y. Zhao, H. Tang, M. Wang, Ceram. Int. 44 (2018) 18996–19001.
[37] S. Xu, M. Wang, L. Qiao, Y. Ye, G. Jia, Y. Zhao, Adv. Appl. Cream. 114 (2015) 256–260.
[38] Z.J. Yang, W.B. Feng, X.Q. Liu, X.L. Zhu, X.M. Chen, J. Am. Ceram. Soc. 102 (2019) 4721–4729.
[39] S.H. Jhi, J. Ihm, S.G. Louie, M.L. Cohen, Nature 399 (1999) 132–134.
[40] X. Cai, L. Zhong, Y. Xu, Z. Lu, J. Li, J. Zhu, Y. Ding, H. Yan, J. Alloys Compd. 747 (2018) 8–20.
[41] F. Rezaei, M.G. Kakroudi, V. Shahedifar, N.P. Vafa, M. Golrokhsari, Ceram. Int. 43 (2017) 3489–3494.
[42] K. Hackett, S. Verhoef, R.A. Cutler, D.K. Shetty, J. Am. Ceram. Soc. 92 (2009) 2404–2407.
[43] D. Demirskyi, Y. Sakka, O. Vasylkiv, Ceram. Int. 41 (2015) 10828–10834.
[44] L. Cheng, Z. Xie, G. Liu, W. Liu, W. Xue, J. Eur. Ceram. Soc. 32 (2012) 3399–3406.
[45] Y. Gu, J. Liu, F. Xu, G. Zhang, J. Eur. Ceram. Soc. 37 (2017) 539–547.
[46] M. Sribalaji, B. Mukherjee, A. Islam, A.K. Keshri, Mater. Sci. Eng. A 702 (2017) 10–21.
[47] A. Nino, A. Sasago, S. Sugiyama, H. Taimatsu, Int. J. Refract. Metals Hard Mater. 61 (2016) 192–200.
[48] H. Kim, I. Shon, J. Yoon, S. Lee, Z.A. Munir, Int. J. Refract. Metals Hard Mater. 24 (2006) 202–209.
[49] A. Gubernat, P. Rutkowski, G. Grabowski, D. Zientara, Int. J. Refract. Metals Hard Mater. 43 (2014) 193–199.
[50] C. Peng, H. Tang, Y. He, X. Lu, P. Jia, G. Liu, Y. Zhao, M. Wang, J. Mater. Sci. Technol. 51 (2020) 161–166.
[51] J. Cabrero, F. Audubert, R. Pailler, J. Eur. Ceram. Soc. 31 (2011) 313–320.
[52] Z. Fu, L. Jiang, J.L. Wardini, B.E. Macdonald, H. Wen, W. Xiong, D. Zhang, Y. Zhou, T.J. Rupert, W. Chen, E.J. Lavernia, Sci. Adv. 4 (2018) eaat8712.
[53] S. Jiang, H. Wang, Y. Wu, X. Liu, H. Chen, M. Yao, B. Gault, D. Ponge, D. Raabe, A. Hirata, M. Chen, Y. Wang, Z. Lu, Nature 544 (2017) 460–464.
[54] T. Yang, Y.L. Zhao, Y. Tong, Z.B. Jiao, J. Wei, J.X. Cai, X.D. Han, D. Chen, A. Hu, J.J. Kai, K. Lu, Y. Liu, C.T. Liu, Science 362 (2018) 933–937.
[55] P.F. Becher, C.H. Hsueh, P. Angelini, T.N. Tiegs, J. Am. Ceram. Soc. 71 (2010) 1050–1061.
[56] Y. He, L. Zhong, F. Fan, C. Wang, T. Zhu, S.X. Mao, Nat. Nanotechnol. 11 (2016) 866–871.
[57] Q. Feng, X. Song, X. Liu, S. Liang, H. Wang, Z. Nie, Nanotechnology 28 (2017) 475709.

Chong Peng
State Key Laboratory of Metastable Materials Science and Technology, Yanshan University, Qinhuangdao 066004, China

Hu Tang*
Academy for Advanced Interdisciplinary Studies, Southern University of Science and Technology, Shenzhen 518055, China

Changjian Geng, Pengjie Liang
State Key Laboratory of Metastable Materials Science and Technology, Yanshan University, Qinhuangdao 066004, China

Biao Wan
Key Laboratory of Material Physics, Ministry of Education, School of Physics and Microelectronics, Zhengzhou University, Zhengzhou 450052, China

Yujiao Ke
School of Mechanical Engineering, Yanshan University, Qinhuangdao 066004, China

Yuefeng Wang*, Peng Jia
State Key Laboratory of Metastable Materials Science and Technology, Yanshan University, Qinhuangdao 066004, China

Wenfeng Peng
Center for High Pressure Science and Technology Advanced Research, Beijing 100190, China

Lina Qiao
Hebei Construction Material Vocational and Technical College, Qinhuangdao 066004, China

Kenan Li
State Key Laboratory of Superabrasives, Zhengzhou Research Institute for Abrasives & Grinding Co., Ltd., Zhengzhou 450001, China

Xiaohong Yuan
Academy for Advanced Interdisciplinary Studies, Southern University of Science and Technology, Shenzhen 518055, China

Yucheng Zhao, Mingzhi Wang*
State Key Laboratory of Metastable Materials Science and Technology, Yanshan University, Qinhuangdao 066004, China

*Corresponding authors.
E-mail addresses: tanghu_future@163.com (H. Tang), wangyuefeng@ysu.edu.cn (Y. Wang), wmzw@ysu.edu.cn (M. Wang)
Revised 21 April 2021